

Geant4 Simulation of Scatter Radiation Removal: Comparison and Validation of Anti-scatter Grid and Air Gap for X-ray Mammography

Abdalmajeid M. Alyassin^a, Ali H. Aljarrah^a, Zaid Q. Ababneh^a,
Anas M. Ababneh^a and Noor A. Alyassin^b

^a Physics Department, Yarmouk University, Irbid, Jordan.

^b American Horizon Medical, Watervliet NY, USA..

Doi: <https://doi.org/10.47011/17.1.3>

Received on: 14/03/2022;

Accepted on: 05/10/2022

Abstract: X-ray mammography modality provides excellent low-contrast resolution images with low scatter radiation, making it the gold standard in diagnosing breast cancer. Anti-scatter grid and air gap techniques are typically used to further minimize the scatter radiation and improve image quality. Thus, Geant4 simulation was used to investigate the effectiveness of these techniques in removing scatter radiation in X-ray mammography. The effectiveness of an anti-scatter grid was evaluated using the Bucky factor, where it linearly increased with increasing the anti-scatter grid ratio. It was found that increasing the grid frequency affects the Bucky factor depending on the design of the grid ratio. This research proved that designing an anti-scatter grid with high grid frequency (80 lp/mm), low grid ratio (2:1), and proper orientation minimized common anti-scatter grid artifacts. The effectiveness of the air gap technique was also evaluated using the air gap dose factor. It increased non-linearly with increasing magnification. This research validated that using smaller pixel sizes and small focal spot sizes improved spatial resolution with magnification. Our simulation validated that the anti-scatter grid and air gap were effective techniques in removing scatter radiation. By comparing these techniques, the anti-scatter grid was more effective in removing scatter radiation at the expense of increasing the radiation absorbed dose with the exception of 2.0 magnification. It's recommended to be extremely cautious when using 2.0 magnification or a grid ratio higher or equal to 8:1. These parameters may cause the radiation absorbed dose to be increased by several folds.

Keywords: Geant4, Gate, X-ray mammography, Scatter removal, Anti-scatter grid, Air gap.

1. Introduction

Breast cancer is the most common cancer and the second leading cause of cancer-related deaths among females. Annual and biannual screening for females aged 40 and above has significantly contributed to early detection and improved treatment outcomes [1]. Among the screening modalities, X-ray mammography imaging stands as the gold standard for breast cancer detection

[2]. In X-ray mammography, it's crucial to utilize optimal lower energy X-ray photon spectrums to enhance photoelectric tissue interaction and minimize scatter radiation for better image contrast of breast tissues. X-ray mammography filters are made of materials suitable for the X-ray target material to provide an optimal X-ray mammography spectrum. Thus, they are always

listed together as target-filter. The optimal X-ray spectrum spreads around the characteristic energies of the X-ray target, and the chosen filter should effectively attenuate low-energy X-ray photons to reduce absorbed radiation dose while maintaining image contrast by attenuating high-energy X-rays. The most used types of target-filter in X-ray mammography are molybdenum-molybdenum (Mo-Mo), molybdenum-rhodium (Mo-Rh), rhodium-rhodium (Rh-Rh), tungsten-rhodium (W-Rh), tungsten-silver (W-Ag), among others [3-5].

To further enhance the quality of X-ray mammography images by reducing scatter radiation reaching the image receptor, anti-scatter grid (ASG) and air gap (AG) scatter removal techniques are commonly employed. These techniques contribute to achieving excellent low-contrast resolution in X-ray mammography images. The two fundamental



FIG. 1. The height, the spacing, and the width of the septa are denoted as SH, SS, and SW, respectively. The dark area represents a radiopaque material (e.g. lead), while the light area represents a radio-lucent material (e.g. air).

The air gap technique may also be used to remove X-ray scatter radiation [3]. Keeping an air gap between the image receptor (IR) and the breast causes the scatter radiation to miss the IR. As the gap gets larger, the likelihood of the scattered X-ray radiation missing the IR increases. However, leaving an air gap between IR and the breast magnifies the image, which may cause part of the breast image to extend beyond the IR. To address this, magnification is commonly used to focus on suspected small regions of the breast. It's worth noting that magnification may cause blurring of the objects, especially when the standard focal size is used. Therefore, a small focal spot size is typically used for magnification [3, 6].

In diagnostic X-ray radiology imaging, a certain amount of X-ray radiation must reach the image receptor (IR) to provide adequate optical density and image quality. Using scatter removal techniques, such as an anti-scatter grid or air gap, leads to the reduction of the amount of X-ray radiation reaching the IR that is necessary. Thus, one must always increase the X-ray exposure when using such scatter removal

properties that define the anti-scatter grid are the grid ratio (GR) and the grid frequency (GF). GR is defined as the septa's height (SH) of the grid over the septal spacing (SS) (see Fig. 1). The septa may be made of several radiopaque materials that have high atomic numbers and high mass density (e.g., lead). The spacing between the septa may also be made of several radiolucent materials with low atomic numbers and low mass density (e.g., air) [3].

Grid frequency (GF) is defined as one over the grid period (GP) (see Fig. 1). Note that the septa's width (SW) affects directly GF and not GR. For a fixed GR and SH, increasing the SW reduces GF. However, increasing SW while maintaining GF and SH fixed leads to decreasing SS and increasing GR. With proper adjustments to SH, GR can be maintained constant even as SW increases.

techniques to compensate for the loss of scattered X-ray radiation.

The Monte Carlo simulation is a valuable tool for accurately simulating the production of X-rays in many imaging and therapeutic applications [7-11]. Geant4 Application for Tomographic Emission (GATE) made the simulation even more accessible to many end-user researchers, eliminating the need for sophisticated software development [12-16]. Simulating X-ray mammography with Geant4 application is of great interest to many researchers who don't have access to clinical machines. Additionally, simulation allows the testing and study of various configuration parameters without additional cost.

Several published studies have simulated X-ray mammography and the effect of scatter removal techniques [17-21]. One method used a pencil beam and was focused on image processing-based correction techniques [15]. Another study aimed to validate the simulation of dosimetry in mammography phantom using thermoluminescent dosimeters, metal oxide

semiconductor field-effect transistor dosimeters, and GafChromic™ films [18, 19]. Geant4 simulation was also used to study the artifacts generated by the anti-scatter grids in X-ray mammography tomosynthesis, a three-dimensional (3-D) X-ray imaging approach [20]. Geant4 was also used to simulate breast phantoms based on breast CT images and to study issues related to breast phantoms [21]. In addition, some researchers have explored the effect of anti-scatter materials in removing scatter radiation and improving signal-to-noise and other image quality parameters at high X-ray energies [22]. Some studies focused on minimizing post-acquisition scatter radiation using image processing techniques [23]. However, while these techniques are valuable in mitigating scatter radiation effects, they may introduce artifacts or reduce the spatial resolution in the original images.

Therefore, there is a need for further research to test, develop, optimize, validate, and explore the benefits and effectiveness of scatter removal techniques, including anti-scatter grids, air gap, and others [3]. Accordingly, this research will simulate and study an X-ray mammography scanner. In addition, it will validate and compare

X-ray scatter removal techniques utilizing anti-scatter grids and air gap methods.

2. Materials and Methods

In this research, a Monte Carlo Simulation via vGATE (virtual Geant4 Application for Tomographic Emission) using the physics electromagnetic standard-option-3 model was exploited to simulate an X-ray mammography scanner based on its main components, basic geometry, effective energy source, and standard phantoms [8-9, 12-16]. The simulations ran on several low-end personal computers.

2.1. Simulation of X-ray Mammography

The simulation setup consists of a radiation source, a phantom, an anti-scatter grid (ASG), and an image receptor. Unlike the actual X-ray mammography, where the anode focal spot (X-ray energy source) is located opposite the chest wall, the energy source here is located toward the chest wall to simulate better the X-ray intensity distribution [3]. The inverse square law makes the intensity distribution of the X-ray radiation toward the chest wall higher than the intensity toward the nipple area (see Fig. 2) [3].

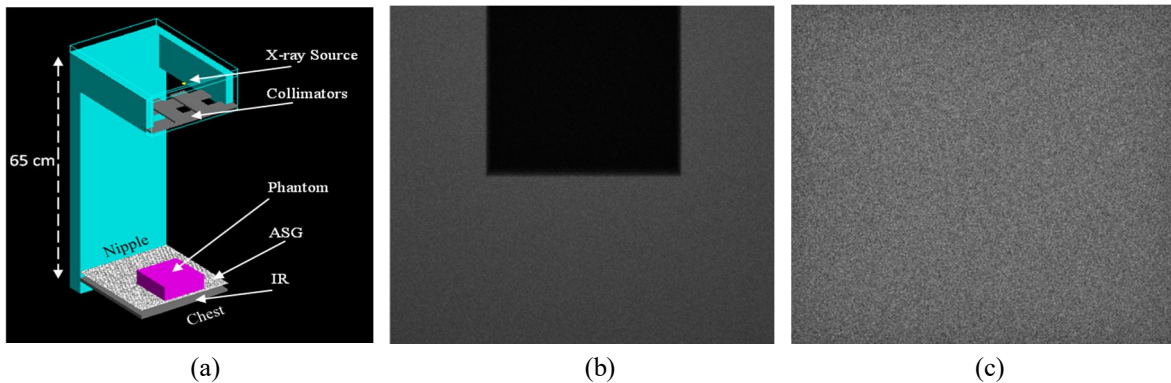


FIG. 2. (a) The simulated X-ray Mammography scanner setup using the acrylic phantom and the anti-scatter grid (ASG) is shown. (b) An image of 1200x1200 pixels covering $24 \times 24 \text{ cm}^2$ where the pixel grey values represent the number of X-ray photons reaching the image receptor (IR) is displayed. (c) An image of 550x550x1 voxels covering $11 \times 11 \times 4 \text{ cm}^3$ is shown. The voxel grey values represent the radiation absorbed values in each voxel.

The shape of the energy source was modeled as planar with a size of $0.3 \times 0.3 \text{ mm}^2$ and $0.1 \times 0.1 \text{ mm}^2$ for standard and magnification acquisitions, respectively. The source was modeled to emit polygenetic X-ray photons covering the image receptor (IR). The source was shielded by lead from all directions except for a window defined by the collimator that exposed the image receptor. The vertical distance between the source and image receptor was made to be 65 cm (see Fig. 2). Two phantoms were used in our

simulation, the acrylic phantom and the line pair spatial resolution phantom. The acrylic phantom had dimensions of $11 \times 11 \times 4 \text{ cm}^3$. The center of the acrylic phantom without additional air gap was located 60.75 cm vertically away from the center of the radiation source. This generated a minimum air gap of 2.25 cm between the bottom of the phantom and the IR. This space was allocated for the ASG. The center of the ASG was located vertically 63.25 cm away from the center of the energy source. The area of the ASG

covered $24 \times 24 \text{ cm}^2$ with different heights according to the ASG design. The top of the IR was located 65 cm vertically from the X-ray source. The $24 \times 24 \times 1 \text{ cm}^3$ of IR was made of lead for maximum quantum efficiency.

2.2. Beam Quality

The X-ray spectrums that are typically reshaped and optimized by the filters in an X-ray mammography scanner were modeled by X-ray spectrums that provided similar half-value layers. These spectrums depend on the target and the filter materials. Therefore, the simulated spectrums are named by target-filter materials as follows: molybdenum-molybdenum (Mo-Mo), molybdenum-rhodium (Mo-Rh), tungsten-rhodium (W-Rh), and tungsten-silver (W-Ag). The targets represented the materials of the anode focal spot in an X-ray tube and the filters were represented by properly selected materials. These filter materials were selected to minimize the attenuation of all the X-rays emitted by the target that have energies within the X-ray characteristic photons while maximizing the attenuation of all other X-ray photons [3]. In addition, our modeled energy spectrums compensated for the filtration of the compression paddle and the breast support, typically used in X-ray mammography. In other words, our modeled spectrums simulated the X-ray mammography spectrums with all types of filtrations included.

The simulated X-ray spectrums were made to be of a Gaussian shape that best matched the published spectrums [3]. The half-value layers (HVL) for these spectrums were measured in our simulation using a standard technique of narrow beam geometry with several acquisitions with different aluminum thicknesses [3]. In diagnostic X-ray radiology, the HVL is an effective indicator of the X-ray beam energy quality where the effective beam quality increases with increasing the HVL [3].

TABLE 1. The parameters used in the ASG simulations with the five GRs for each of the septa spacing (SS) % of the grid period (GP) are listed. GF was set to 80 lp/cm and GP was equal to 0.125 mm.

SS% of GP	SS (mm)	SW (mm)	SH (mm)	Grid Ratio
50%	0.0625	0.0625	0.125, 0.250, 0.3125, 0.500, 0.625	2:1, 4:1, 5:1, 8:1, 10:1
60%	0.075	0.05	0.150, 0.300, 0.375, 0.600, 0.750	2:1, 4:1, 5:1, 8:1, 10:1
73%	0.090909	0.034091	0.181818, 0.363636, 0.454545, 0.727272, 0.909090	2:1, 4:1, 5:1, 8:1, 10:1
75%	0.09375	0.03125	0.1875, 0.3750, 0.46875, 0.7500, 0.9275	2:1, 4:1, 5:1, 8:1, 10:1
80%	0.1	0.025	0.2, 0.4, 0.5, 0.8, 1.0	2:1, 4:1, 5:1, 8:1, 10:1

GP is the grid period, SS is septa spacing, SW is septa width, and SH is septa height.

Additionally, the radiation absorbed dose distribution was simulated. An acrylic phantom with dimensions of $11 \times 11 \times 4 \text{ cm}^3$ was used to simulate a typical breast size. The simulated X-ray mammography scanner without the use of ASG was used to image the acrylic phantom. Our simulation was executed using each of the four simulated X-ray spectrums with 100 million photons. We employed vGATE simulation to calculate several parameters in our acquisitions. The main calculated parameters are the number of photons and the radiation absorbed dose stored in IR and the acrylic phantom. These values were stored as images (see Fig. 2). The resolution of the image receptor was controlled by the user. The IR was set to 1200×1200 pixels covering the $24 \times 24 \text{ cm}^2$ full field of view, as seen in Fig. 2(b). The phantom was voxelated to $550 \times 550 \times 40$ voxels. Each voxel dimension was set to $0.2 \times 0.2 \times 1 \text{ mm}^3$. Thus, there were forty 1-mm thick slices. Slice 1 represented the surface of the phantom and slice 40 represented the bottom of the phantom. ImageJ software application was used to view the images and to calculate the radiation absorbed dose for each slice of the acrylic phantom [24, 25]. Figure 2(c) shows a vertical summation projection image of all radiation-absorbed dose values through the slices of the acrylic phantom.

2.3. Scatter Radiation Removal Using Anti-Scatter Grid

2.3.1. Grid Ratio

The ASG was simulated by keeping the grid frequency (GF) fixed while changing GR. In this simulation, the effect of septa spacing (SS) contribution to the grid period (GP) in removing scatter radiation was also studied. Similarly, these simulations can be used to study the effect of septa width (SW) contribution to GP in removing scatter radiation since SW% is equal to 100% minus SS%.

The ASG with five different contributions of SS from GP was simulated. The simulated SS% of GP were 50%, 60%, 73%, 75%, and 80% (see Table 1). Five GRs for each of the simulated SS% were generated (see Table 1). A GF of 80 lp/cm (GP of 0.125 mm) was used for all of these simulations. Table 1 shows that SW, SS, and SH have values according to GRs and GFs.

Our simulation was executed with and without the use of ASG using 10 million primary photons in imaging the acrylic phantom. The W-Ag energy spectrum was used for the energy source in these simulations. The number of detected photons in the image receptor (IR) without grid (NWoG) and the detected number of photons in the IR with grid (NWG) was measured. Then, the ratio of NWoG / NWG for all ASG designs at the specified GRs was calculated.

Using a septa spacing (SS) equal to 50% of the period of the ASG, the simulation was repeated to estimate the Bucky factor of the acrylic phantom. Five ASGs with different grid ratios (GR) at the same grid frequency (GF) of 40 lp/cm were simulated. In this design, the values of SS and SW were each equal to 0.125 mm. The septa heights (SH) of the ASG with GR of 2:1, 4:1, 5:1, 8:1, and 10:1, were 0.25, 0.5, 0.625, 1.0, and 1.25 mm, respectively.

Ten million photons were used to emanate from the W-Ag energy source in each of the simulations. Firstly, without using any ASG, the radiation absorbed dose in the acrylic phantom (DwoG) and the number of photons deposited in the IR (NWoG) were calculated. The simulation was re-executed using the ASG and calculated the number of photons deposited in the IR (NWG). Secondly, the multiplier factor was calculated to be equal to the ratio of NWoG / NWG. This ratio was multiplied by ten million

photons to compensate for the possible loss of X-ray scatter radiation when ASG is used. This step provides the required number of photons needed for adequate optical density or image quality. The simulation was repeated using the modified number of photons with the use of ASG. The modified radiation absorbed dose (MDWG) of the acrylic phantom was then calculated. The Bucky factor was estimated as the MDWG with the use of ASG over the estimated DwoG without the use of ASG. Finally, this simulation was repeated using the ASG with GRs of 2:1, 4:1, 5:1, 8:1, and 10:1.

2.3.2. Grid Frequency

In this simulation, SS 50% of GP was used in simulating several grid frequencies (GFs). The effect of changing GF in two different manners was studied. In the first simulation, GR to 4:1 was fixed while changing GP. Table 2 shows all the parameters used to generate GF of 20, 40, 50, and 80 lp/cm. The simulation was re-executed with these GSs using ten million photons emanating from the W-Ag energy source. Next, the radiation absorbed dose without grid (DwoG) and the ratio of NWoG/NWG were estimated, as described earlier. The ratio of NWoG/NWG was multiplied by ten million photons to estimate the modified number of photons. Using the modified number of photons in our simulation, the modified absorbed dose with grid (MDWG) was calculated. Finally, the Bucky factor was calculated as MDWG with the use of ASG over the DwoG without the use of ASG for each GF.

In the second simulation, the selected GFs were generated by fixing the height of the ASG while changing the GP according to the desired GF. In this technique, the GR changed as well. Table 2 shows the parameters of the ASG used in this simulation.

TABLE 2. The parameters of the ASG with different simulations of GF are shown. The simulations consisted of changing GF with constant GR and changing GF with fixing septa height (SH).

Simulation	GF (lp/mm)	SH (mm)	SS = SW (mm)	Grid Ratio
Fixed GR	20, 40, 50, 80	1, 0.5, 0.4, 0.25	0.25, 0.125, 0.1, 0.0625	4
Fixed SH	20, 40, 50, 80	0.5	0.25, 0.125, 0.1, 0.0625	2, 4, 5, 8

GF is the Grid Frequency, SH is septa's height, SS is septa spacing, and septa's width.

2.3.3. Artifacts

There are two types of artifacts that may be generated due to the usage of ASG, the periodic and the shadowing artifacts. The periodic artifact is caused by the grid's periodicity of ASG. If GF

is lower than the spatial frequency resolution of the image receptor, then this may make SW larger than the pixel size. Thus, some pixels will be blocked from radiation by SW, causing a periodic pattern on IR.

In digital X-ray mammography, the minimum spatial frequency resolution that is accepted by the Mammography Quality Standard Act (MQSA) is 5 lp/mm [3]. This forces the sampling frequency according to the Nyquist sampling theorem to be at least 10 lp/mm. This makes the pixel size to be at most 0.1 mm. Since the field of view in our simulation was 24x24 cm², then IR must consist of at least 2400x2400 pixels to fulfill the MQSA regulation.

To validate the periodicity artifact, our acrylic phantom was scanned with ASG of three different GFs: 20, 40, and 80 lp/cm. The periods for these GFs corresponded to 0.5, 0.25, and 0.125 mm, respectively. Using ASG with SS 50% of GP, SW, and SS were equal to 0.25, 0.125, and 0.0625 mm, respectively. For a GR of 4:1, the SHs of ASG were equal to 1.0, 0.5, and 0.25 mm, respectively. In this set of simulations, 100 million photons were used.

The effect of IR spatial resolution on the periodic artifact was also studied. With a large pixel size, more radiation will reach IR, causing less ASG artifact. Our simulation was re-executed using ASG with SS 50% of GP, GF of 20 lp/mm, and GR 4:1 with a different IR spatial resolution. The IR had pixel sizes of 0.05, 0.1, 0.2, 0.4, and 0.8 mm. The produced images were 4800x4800, 2400x2400, 1200x1200, 600x600, and 300x300 pixels, respectively.

The source of the shadowing artifact is related particularly to the usage of parallel grids which are used in this study. Based on our scanner geometry, the focal spot size produced a vertically truncated rectangular pyramid radiation beam. The source of radiation emanated from the focal spot (same side as the chest wall) toward the nipple area. SH of ASG plays a major role in causing the shadowing artifact by blocking more radiation toward the nipple area than the chest. SH blocks the radiation from reaching a portion or all of SS. This effect increases the area that does not receive radiation. SH blockage increases in the direction from the chest toward the nipple of the breast. Recall that the SH depends on GR. Therefore, it's expected that as GR increases, the shadowing artifact will also increase. One way to change the shadowing orientation and reduce the influence of this artifact is to change the orientation of septa lines in ASG from perpendicular to being parallel to the chest-nipple axis.

The effect of GR on the blockage of radiation (shadowing artifact) was studied toward the nipple area on IR. Our acrylic phantom was scanned using ASG with SS 50% of DP, GF of 80 lp/cm, and ran our simulation with ASG of GR of 2:1, 4:1, and 8:1. The pixel size in the IR was set to 0.1 mm and 100 million photons were used. The acrylic phantom was scanned twice. In the first scan, the septa's alignment was perpendicular to the chest-nipple axis, while in the second scan, the septa's alignment was parallel to the chest-nipple axis.

2.3.4. Scatter Radiation Removal Using Air Gap

Depending on each slice location in the phantom, magnification without additional air gap ranges between 1.034 to 1.106. This magnification is higher than one because the acrylic phantom has a height of 4 cm and there is always a gap between the bottom of the phantom and the image receptor. This minimum magnification occurs due to an air gap of 2.25 cm between the bottom of the phantom and the image receptor. Recall that this gap was allocated for the placement of the ASG. The slices located at the bottom, the center, and the top of the phantom have magnifications of 1.034, 1.067, and 1.106, respectively.

The typical image magnifications used in X-ray mammography are 1.2, 1.5, 1.8, and 2.0 [3]. In our simulation, the acrylic phantom was positioned to give us these magnifications at the center of the phantom. An air gap of 8.83 cm provided a magnification of 1.2 at the center slice of the phantom, with a magnification range of 1.157-1.246 for the remaining slices of the phantom. An air gap of 19.67 cm provided a magnification of 1.5 at the center slice of the phantom, with a range of 1.434 to 1.573 for the remaining slices. An air gap of 26.89 cm provided a magnification of 1.8 at the center slice of the phantom, with a range of 1.706 to 1.906 for the remaining slices. Also, an air gap of 30.5 cm provided a magnification of 2.0 at the center slice of the phantom, with a 1.884-2.131 range for the other slices.

2.3.5. Beam Quality

Our simulation was executed with several air gaps to assess their effectiveness in scatter removal radiation and the possible additional radiation absorbed dose that they may cause. Based on the radiation inverse square law, it's

expected that as the breast moves closer to the source (to be magnified) the radiation absorbed dose will be higher. Also, different slice locations in the phantom have different magnifications, as mentioned earlier. The closer the slice location is to the radiation source, the higher the magnification. Furthermore, in X-ray mammography, the size of the phantom image is slightly bigger than the actual phantom size due to geometry magnification.

The simulations were run at five air gap settings, 1.067 (no gap), 1.2, 1.5, 1.8, and 2.0, using four simulated energy sources (Mo-Mo, Mo-Rh, W-Rh, and W-Ag). Ten million photons were emitted from each source in these simulations. First, the simulation was executed and the number of photons that reached the image receptor without additional air gap (NWoAG) and the radiation absorbed dose (DWoAG) to the phantom were calculated. Then, the simulations were re-executed with the air gaps and the number of photons that reached the image receptor (NWAG) and the radiation absorbed dose to the phantom (DWAG) were calculated. The multiplier factor of (NWoAG/NWAG) that was used to modify the number of photons emitted from the source was calculated. With the new modified number of photons, our simulations were re-executed with the selected AG, and the modified radiation absorbed dose to the phantom (MDWAG) was calculated. Then, the air gap dose factor (AGDF) was calculated as (MDWAG/DWoAG).

2.3.6. Spatial Resolution

Although air gap (magnification) is an effective technique for removing scatter radiation, two factors associated with magnification may either worsen or improve the spatial resolution. The factor that may worsen the spatial resolution is the blurring of the objects that occurs due to the focal spot size of the X-ray source. The spatial resolution deteriorates as the size of the source increases [3]. However, the factor that may improve the spatial resolution with magnification is the increase in the number of samples for small objects. Magnification in X-ray mammography is typically used to focus and image a small region of the breast. Therefore, there will be more pixels representing these smaller regions, which will make them look bigger and may have enough representation on the image receptor.

A line pair phantom was developed to test spatial frequency resolution of 0.25, 0.5, 1.0, 2.0, 4.0, 5.0, 6.0, and 7.0 lp/mm. This line pair phantom was simulated from lead and air for each line pair. Each frequency was repeated for approximately 6 mm covering the 4.8 cm length of the line pair phantom. The width and the height of the phantom were set to 1 cm and 0.07 mm, respectively. Therefore, the periods of the spatial resolution 7, 6, 5, 4, 2, 1, 0.5, 0.25 lp/mm were repeated 41, 35, 30, 24, 12, 6, 3, and 1 time/s, respectively.

The effect of the air gap (magnification) on spatial resolution was tested by scanning the line pair phantom and placing it directly on the image receptor (no magnification). Then, the line pair phantom was scanned with the magnification of 1.5 and 2.0 with similar parameters. One hundred million photons, a W-Ag energy source size of $0.1 \times 0.1 \text{ mm}^2$, and IR with a pixel size of $0.15 \times 0.15 \text{ mm}^2$ were used. The acquired simulated images were viewed with ImageJ software and visually assessed the spatial frequency resolution that was visible from the line pair phantom [24].

The effect of the source size was also tested on the spatial resolution by scanning the line pair phantom with two source sizes of $0.3 \times 0.3 \text{ mm}^2$ and $0.1 \times 0.1 \text{ mm}^2$. The pixel size of $0.15 \times 0.15 \text{ mm}^2$ and the magnification of 2.0 were kept for both cases. The images were visually inspected for spatial frequency resolution using ImageJ software.

Lastly, the effect of the pixel size in the IR was tested on the spatial resolution by using the following pixel sizes: $0.15 \times 0.15 \text{ mm}^2$, $0.1 \times 0.1 \text{ mm}^2$, and $0.0625 \times 0.0625 \text{ mm}^2$. The source size of $0.1 \times 0.1 \text{ mm}^2$ and the magnification of 1.5 were kept fixed between these three simulations. The spatial frequency resolution was visually assessed by viewing the images using ImageJ software.

2.4. Comparison of Scatter Radiation Removal Techniques

Several parameters affect each scatter removal technique. For the ASG technique, GR, GF, and SW are the main parameters that directly affect the ASG performance in removing X-ray scatter radiation and may cause artifacts. For the AG technique, however, the magnification factor and the focal spot size

affect the AG performance in removing X-ray scatter radiation and may cause artifacts. A general comparison in the percent scatter removal and the increase in the radiation absorbed dose for both the anti-scatter grid and air gap, helps us make valid assumptions and recommendations. The percent scatter removal was estimated for ASG as the difference between the number of photons that reached the IR without ASG (NWoG) minus the number of photons that reached the IR with ASG (NWG) over the NWoG all multiplied by 100. Similarly, the percent scatter removal was estimated for AG as the difference between the number of photons that reached the IR without AG (NWoAG) minus the number of photons that reached the IR with AG (NWAG) over the NWoAG all multiplied by 100. These measurements were taken from previous simulations. The results of using ASG with GR of 2, 4, 5, and 8 at GF of 40 lp/mm and the results of using AG with a magnification of 1.2, 1.5, 1.8, and 2.0 were used in this comparison. The Bucky factor for ASG and the AGDF for AG was used to compare the radiation absorbed dose in the acrylic phantom.

3. Results and Discussions

3.1. Beam Quality

The results of our four simulated X-ray energy sources and their half-value layers are

TABLE 3. The HVLs, the means, and standard deviations for the simulated X-ray energy spectrums are listed.

Energy Source Target-Filter	Mean (keV)	Standard Deviation (keV)	*HVL (mm) Aluminum
Mo-Mo spectrum	15.5	5.9	0.35
Mo-Rh spectrum	17.5	8.8	0.45
W-Rh spectrum	17.7	6.6	0.55
W-Ag spectrum	18.1	8.9	0.65

* HVL is the half value layer in Aluminum

3.2. Scatter Radiation Removal Using Anti-Scatter Grid

3.2.1. Grid Ratio

Table 4 and Fig. 3 show the ratio of the detected photons in the image receptor (IR) without grid (NWoG) versus the detected photons in IR with the use of grid (NWG). Note as the GR increased, more scattered photons were removed, and the ratio of NWoG/NWG was increased. The rate of increase in the ratio

summarized in Table 3. The shape of the Mo-Mo simulated X-ray beam spectrum was a normalized Gaussian with a mean of 15.5 keV and a standard deviation of 5.9 keV. This distribution closely resembles that of a 30 keV high voltage using a Mo target with a 0.03 mm Mo filter [3]. The measured half-value layer (HVL) for the Mo-Mo spectrum was 0.35 mm of aluminum (Al). Also, the shape of the Mo-Rh simulated X-ray beam spectrum was a normalized Gaussian with a mean of 17.5 keV and a standard deviation of 8.8 keV. This is assumed to resemble best a 30 keV high voltage and a Mo target with a 0.025 mm Rh filter [3]. The measured half-value layer (HVL) for the Mo-Rh spectrum was 0.45 mm of Al. Furthermore, the shape of the W-Rh simulated X-ray beam spectrum was a normalized Gaussian with a mean of 17.7 keV and a standard deviation of 6.6 keV. The measured half-value layer (HVL) for the W-Rh spectrum was 0.55 mm of Al. In addition, the shape of the W-Ag simulated X-ray beam spectrum was a normalized Gaussian with a mean of 18.1 keV and a standard deviation of 6.9 keV. The measured half-value layer (HVL) for the W-Ag spectrum was 0.65 mm of Al. Note the higher the mean energy, the higher the HVL (see Table 3).

was more dominant for lower septa's spacing (i.e. 50% of GP) (see Fig. 3). This was validated by the slopes in Fig. 3. The lower the percent of SS of GP, the higher the slope and the higher the scatter radiation removal were observed. Note also for a fixed GR, the lower the SS % of GP the less radiation registered into the IR and thus the higher the Bucky factor. The linear regression R^2 for all the fitted slopes in Fig. 3 was higher than 0.999.

TABLE 4. The numbers of detected photons by the image receptor (IR) are listed without (NWoG) and with (NWG) grid at GF = 80 lp/mm for the different GRs. The NWoG was equal to 1 775 808.

GR	SS 50% of GP		SS 60% of GP		SS 73% of GP		SS 75% of GP		SS 80% of GP	
	NWG	$\frac{NWoG}{NWG}$								
2	589342	3.0	694347	2.6	828253	2.1	851801	2.1	905106	2.0
4	276853	6.4	324336	5.5	386466	4.6	397554	4.5	422439	4.2
5	205128	8.7	242532	7.3	289553	6.1	298229	6.0	317424	5.6
8	124883	14.2	148905	11.9	178975	9.9	184676	9.6	196539	9.0
10	100517	17.7	119777	14.8	144314	12.3	148799	11.9	158512	11.2

NWoG is the number of detected photons without a grid, NWG is the number of detected photons with a grid, SS is septa spacing, GR is the grid ratio, and GP is the grid period.

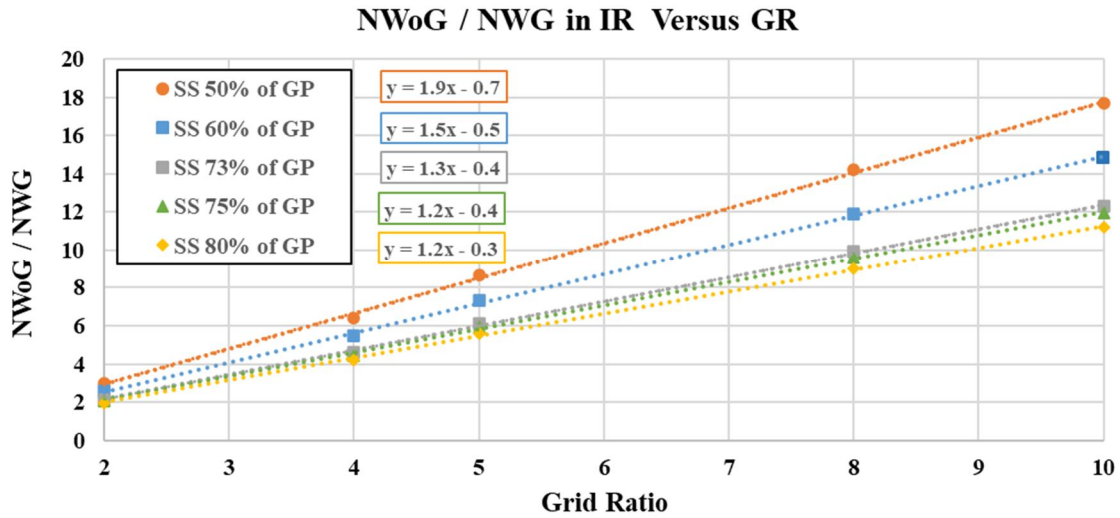


FIG. 3. The ratio of the number of detected photons by the image receptor (IR) without grid (NWoG) over the number of detected photons with grid (NWG) is shown versus grid ratio (GR) for all five (septa's spacing) SS% of GP and GF = 80 lp/mm.

Table 5 shows the results of the Bucky factor using the W-Ag source. Table 5 shows that the ratio of NWoG/NWG matches very well with the Bucky factor. This confirms the linear relationship between the radiation X-ray exposure and the radiation absorbed dose. Note

that the Bucky factor increased linearly with increasing the GR. This indicates the higher the GR, the higher the radiation absorbed dose to the phantom, which also means higher scatter radiation removal [23].

TABLE 5. The estimated Bucky factors for different numbers of photons are shown from a W-Ag simulated source and different grid ratios at GF = 40 lp/cm.

Grid Ratio	Image Receptor		Phantom		Bucky Factor
	No. of Photons		Dose(μ Gy)		
	NWoG	NWG	DWoG	MDWG	
2	1775808	556986	2.58E-03	8.24E-03	3.2
4		258717		1.77E-02	6.9
5		195328		2.32E-02	9.0
8		122008		3.76E-02	14.6
10		98547		4.65E-02	18.0

Source = W-Ag, Emitted No. of photons = 10^7 , Grid Frequency = 40 lp/cm

NWoG: Number of photons in IR without the ASG

NWG: Number of photons in IR with the ASG

DWoG: dose without grid, MDWG: modified dose with grid

Bucky Factor = MDWG / DWoG

3.2.2. Grid Frequency

Table 6 shows GF varies with fixed GR. The Bucky factor decreases slightly with increasing GF. Both SH and SS were changing to maintain the same GR of 4:1. SH was decreasing, which requires the Bucky factor to decrease as well. However, SS was also decreasing, requiring the Bucky factor to increase. This counter effect caused the slow decrease in the Bucky factor as GF increased (see Fig. 4 and Table 6). Note here the rate of decrease is small. This also indicates

that the SH of ASG is more influential than the SS in scatter radiation removal.

For a fixed SH, Table 7 shows that as GF increases, the Bucky factor increases as well. Recall that in this simulation, the height of ASG was fixed while changing SW and SS equally. In this simulation, as the period of ASG decreases (increasing the GF), the GR increases and the Bucky factor increases as well. The effect of changing GR is clearly shown in Fig. 4 and is higher with higher GF.

TABLE 6. The Bucky factor changes with grid frequencies (GF) keeping the grid ratio fixed.

GF	Image Receptor		Phantom		Bucky Factor
	No. of Photons		Dose (μGy)		
	NWoG	NWG	DWoG	MDWG	
20	1775808	251958	2.58E-03	1.82E-02	7.05
40		258717		1.77E-02	6.87
50		263216		1.74E-02	6.75
80		276853		1.69E-02	6.53

Source = W-Ag and Grid Ratio = 4:1

NWoG: number of detected photons without a grid

NWG: the number of detected photons with a grid

DWoG dose without the use of a grid, MDWG is the modified dose with the use of a grid

Bucky Factor = MDWG / DWoG

TABLE 7. The Bucky factor changes with changing grid ratios (GR) and grid frequencies (GF) while keeping the height of the septa fixed.

GR	GF	Image Receptor		Phantom		Bucky Factor
		No. of Photons		Dose (μGy)		
		NWoG	NWG	DWoG	MDWG	
2	20	1775808	541771	2.58E-03	8.47E-03	3.28
4	40		258717		1.77E-02	6.87
5	50		198083		2.32E-02	8.97
8	80		124883		3.67E-02	14.23

Source W-Ag and Septa's Height (SH) = 0.5 mm

NWoG: number of detected photons without grid

NWG: the number of detected photons with grid

DWoG dose without the use of a grid, MDWG is the modified dose with the use of grid

Bucky Factor = MDWG / DWoG

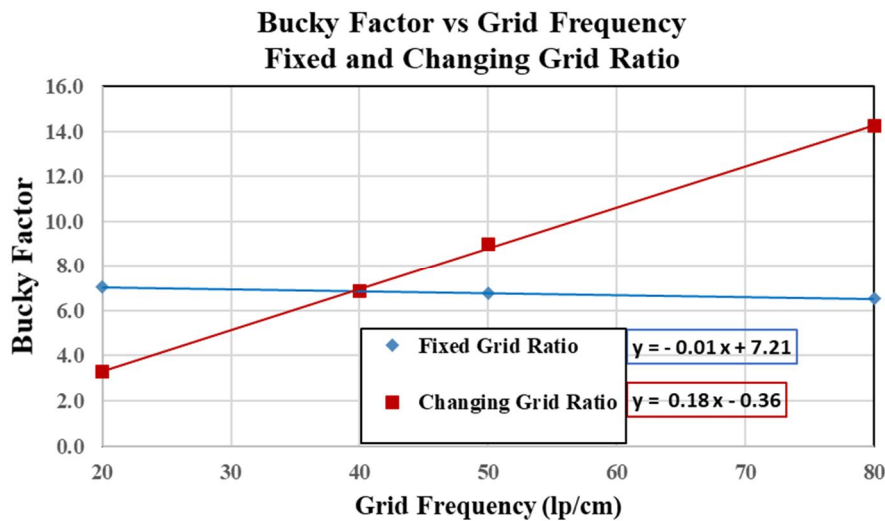


FIG. 4. The Bucky factor changes with changing GR and GF while keeping the height of the septa fixed.

3.2.3. Artifacts

Fig. 5 clearly shows the periodic artifact for lower GF. However, as GF increases, the periodic artifact decreases, as depicted in Figs. 5(b) and 5(c). Note that the shadowing artifacts persist even though the GF has increased. This is due to the usage of parallel anti-scatter grids with the relatively short distance between the energy source and the IR which in this

simulation is equal to 65 cm. Recall the X-ray beam is emitted in a vertically truncated pyramid shape and not parallel.

Fig. 6 shows the periodic artifact is dominant in the high-resolution IR (small pixel size). The larger the pixel size (lower resolution), the less apparent is this artifact. Note that the shadowing artifact persists on the images and does not depend on the IR spatial resolution.

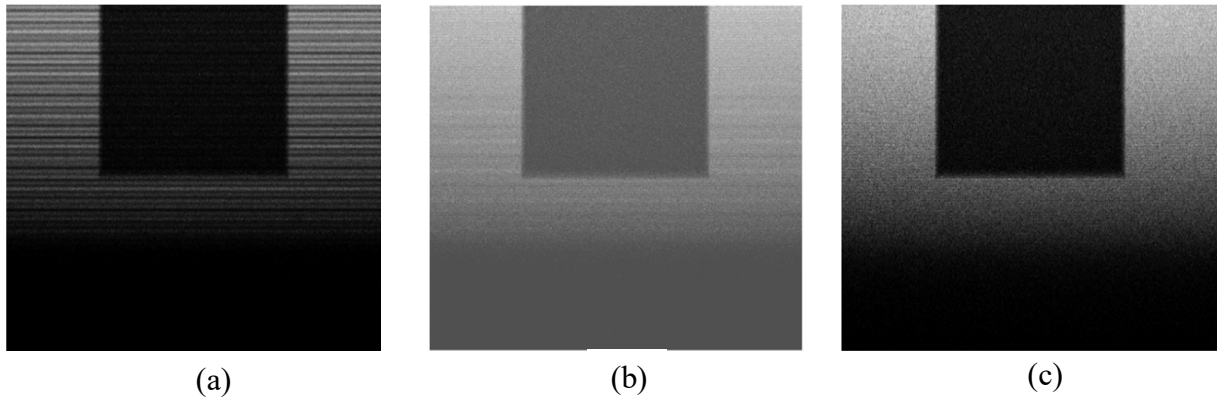


FIG. 5. These images were acquired using IR with a pixel size of 0.1 mm, and ASG with SS = 50% of the GP. (a) The GF = 20 lp/cm and GR = 4:1, (b) The GF = 40 lp/cm and GR = 4:1, and (c) The GF = 80 lp/cm and GR = 4:1.

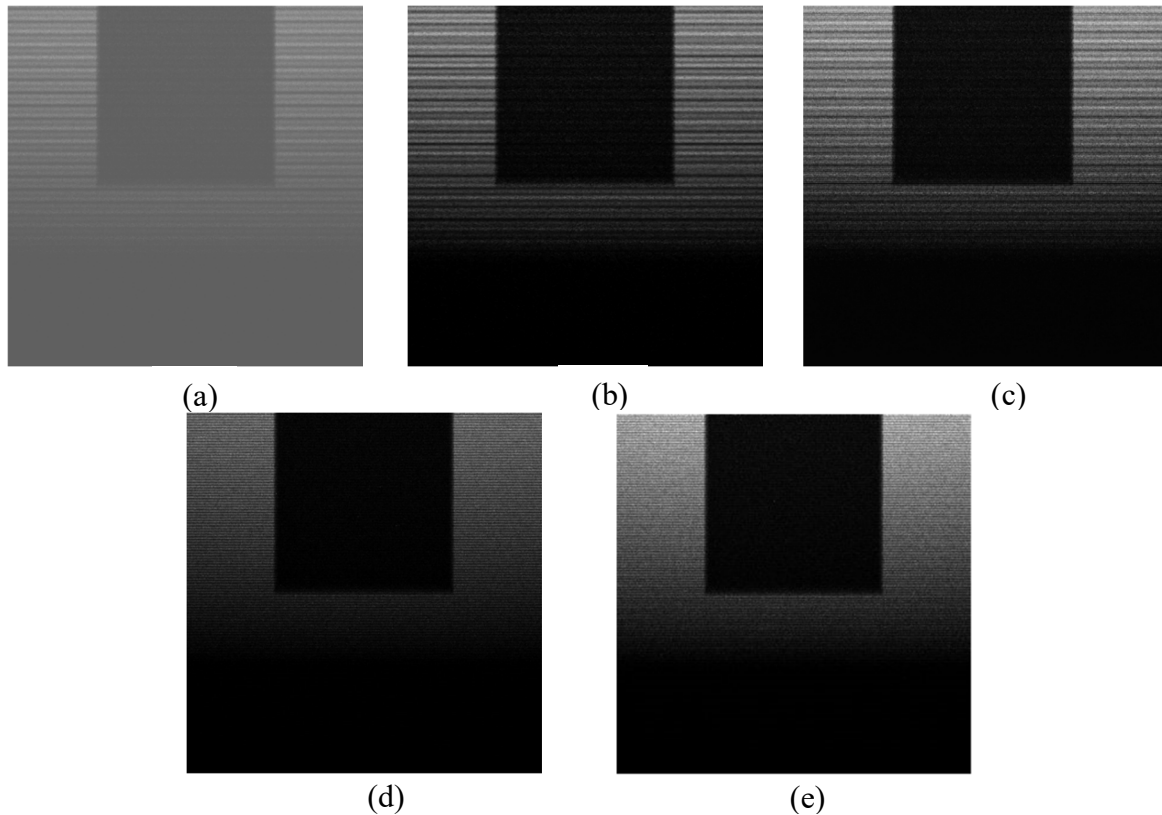


FIG. 6. The images of the acrylic phantom were acquired with SS = 50% of GP using GF = 20 lp/cm and GR 4:1 with different IR pixel sizes. The pixel sizes were equal to (a) 0.05 mm, (b) 0.1 mm, (c) 0.2 mm, (d) 0.4 mm, and (e) 0.8 mm.

Fig. 7 shows the acrylic phantom with very low periodic artifacts due to the usage of high GF (80 lp/cm). However, the shadowing artifact is clearly visible and increases with increasing GR. With high GR, SH is higher which causes more blockage of radiation, causing more shadowing artifacts. This was seen for both orientations of the ASG septa alignment.

However, the shadowing appeared less when the orientation of the septa's alignment was parallel to the chest-nipple axis, especially at GR of 4:1. Therefore, to minimize both artifacts, it is recommended to use ASG with high GF and low GR and orienting the septa's alignment to be parallel to the chest-nipple axis.

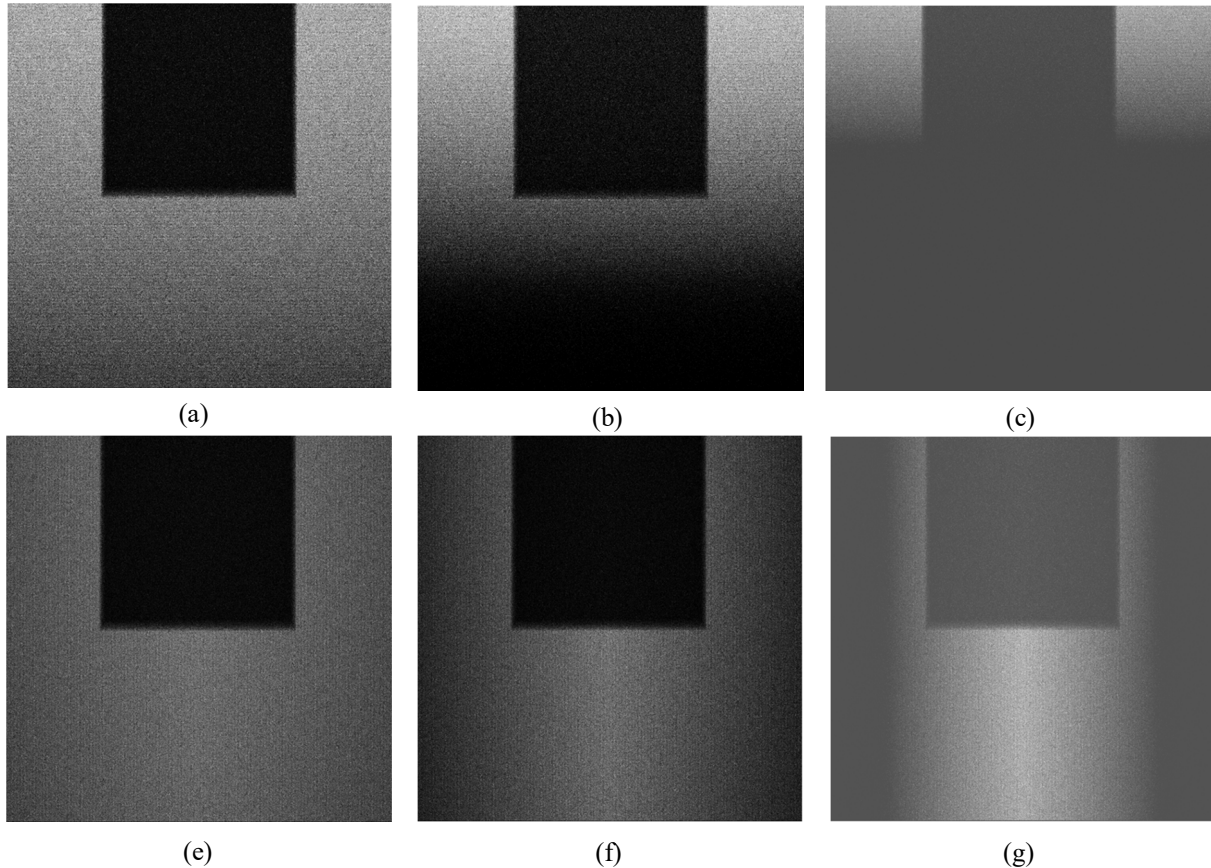


FIG. 7. Images of the acrylic phantom using ASG with GF = 80 lp/cm and IR with a pixel size of 0.1 mm are displayed. In Figs. 7(a), 7(b), and 7(c), the septa were oriented perpendicular to the chest-nipple axis. In Figs. 7(e), 7(f), and 7(g), the septa were oriented parallel to the chest-nipple axis. The GRs for (a) and (e) were equal to 2:1, (b) and (f) were equal to 4:1, and (c) and (g) were equal to 8:1.

3.3. Scatter Radiation Removal Using Air Gap

3.3.1. Beam Quality

Table 8 shows the increase in the scatter radiation removal and the increase in the radiation absorbed dose with higher magnification. Furthermore, the air gap radiation dose factor (AGDF) shows that the radiation absorbed dose to the phantom further increased when using the modified number of photons. Recall that the modified number of emitted

photons is used to compensate for the scatter radiation not reaching the image receptor.

Table 8 and Fig. 8 show that the AGDF is somewhat similar between energy sources, with a magnification factor lower than 1.8. However, for magnifications above 1.8, the differences in AGDF between the sources increase. Indeed, with 2.0 magnification, the Mo-Mo source produced the highest AGDF because of its lower energy. At this magnification, the lower the energy, the higher the absorbed dose was to the phantom.

TABLE 8. The effect of air gap (AG) on the removal of the scatter radiation and the radiation absorbed dose is shown. The simulation was performed using the following energy sources, Mo-Mo, Mo-Rd, W-Rd, W-Ag. 10 million photons were emitted from each source.

Source	Magnification	Image Receptor		Phantom		Phantom		AGDF	
		N.o of Photons	N.o of Photons	Dose (μGy)					
Mo-Mo	1.2	1638189	1490167	2.38E-03	3.02E-03	1.3	3.3E-03	1.4	
	1.5		1085538		4.80E-03		2.0	7.3E-03	3.1
	1.8		601355		6.98E-03		2.9	1.9E-02	8.0
	2.0		235799		8.63E-03		3.6	6.0E-02	25.2
Mo-Rh	1.2	1697521	1547370	2.49E-03	3.16E-03	1.3	3.5E-03	1.4	
	1.5		1145217		5.01E-03		2.0	7.4E-03	3.0
	1.8		665238		7.24E-03		2.9	1.8E-02	7.4
	2.0		302503		8.94E-03		3.6	5.0E-02	20.1
W-Rh	1.2	1738813	1588953	2.58E-03	3.27E-03	1.3	3.6E-03	1.4	
	1.5		1189929		3.82E-03		1.5	7.5E-03	2.9
	1.8		712415		7.44E-03		2.9	1.8E-02	7.0
	2.0		352108		9.18E-03		3.6	4.5E-02	17.6
W-Ag	1.2	1775808	1628025	2.58E-03	3.27E-03	1.3	3.6E-03	1.4	
	1.5		1233111		5.15E-03		2.0	7.4E-03	2.9
	1.8		763247		7.42E-03		2.9	1.7E-02	6.7
	2.0		409407		9.15E-03		3.5	4.0E-02	15.4

NWoAG: number of detected photons without air gap, DWoAG: dose Phantom without air gap
MDWAG: modified dose phantom with an air gap, NWAG: number of detected photons with an air gap
DWAG: dose phantom with air gap, AGDF: air gap dose factor = MDWAG / DWoAG

Air Gap Dose Factor Versus Magnification

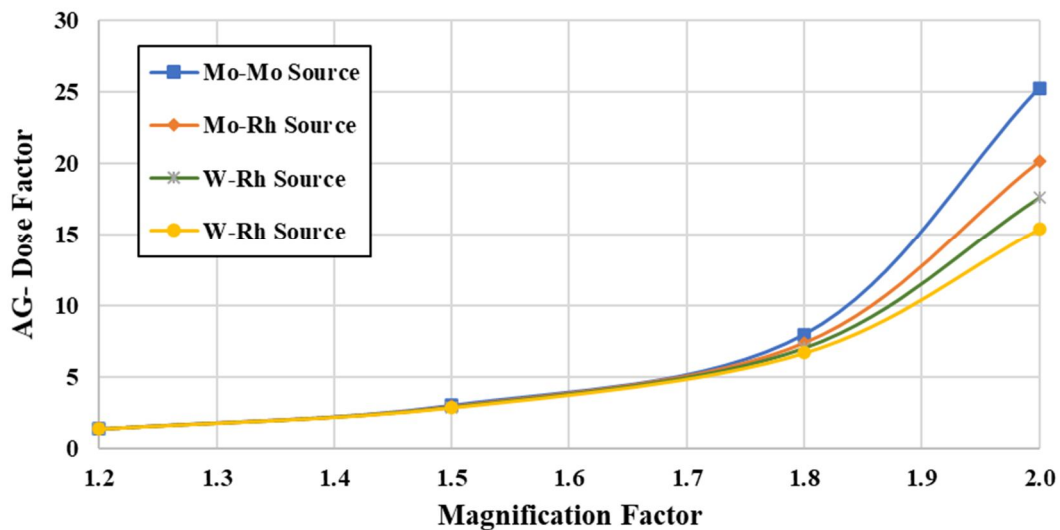


FIG. 8. The effect of magnification on the Air Gap Dose Factor (AGDF) is demonstrated. The rates of increase between the sources are similar except for magnification above 1.8. The increase is inversely proportional to the mean energy of the radiation source.

3.3.2. Spatial Resolution

Fig. 9 shows how the spatial resolution improved as the magnification factor increased from 1.0 to 2.0. Recall that the pixel size was kept at $0.15 \times 0.15 \text{ mm}^2$ and the source size was set to $0.1 \times 0.1 \text{ mm}^2$. A small source size was used to reduce the blurring while magnifying the line pair phantom. This helped some higher-frequency objects to be visible with higher

magnification. For instance, unlike the image acquired with a magnification of 1, shown in Fig. 9(a), the spatial resolution frequency of 4 lp/mm was visible in the image acquired with a magnification of 2.0, as depicted in Fig. 9(b) (see also Table 9).

The spatial resolution improved as the source size decreased from $0.3 \times 0.3 \text{ mm}^2$, illustrated in Fig. 9(c) to $0.1 \times 0.1 \text{ mm}^2$, as seen in Fig. 9(d).

Recall that the magnification was kept at 2.0 and the pixel size was kept at $0.15 \times 0.15 \text{ mm}^2$. Unlike the larger source size, with a smaller source size, the visible spatial resolution frequency was 4 lp/mm (see Fig. 9(d) and Table 9). The spatial resolution improved as the pixel size decreased from $0.15 \times 0.15 \text{ mm}^2$ to $0.1 \times 0.1 \text{ mm}^2$ and then to

$0.0625 \times 0.0625 \text{ mm}^2$. Recall that the source size was kept at $0.1 \times 0.1 \text{ mm}^2$ and the magnification at 1.5. Unlike the larger pixel sizes in Fig. 9(e), with a pixel size of $0.0625 \times 0.0625 \text{ mm}^2$, the visible spatial resolution frequency was 6 lp/mm (see Fig. 9(f) and Table 9).

TABLE 9. The results of the three spatial resolution visual assessments in (lp/mm) of the simulated line pair phantom images are listed. In each experiment, two variables were fixed while changing the third.

Pixel Size = $0.15 \times 0.15 \text{ mm}^2$		Pixel Size = $0.15 \times 0.15 \text{ mm}^2$		Source Size = $0.1 \times 0.1 \text{ mm}^2$	
Source Size = $0.1 \times 0.1 \text{ mm}^2$		Magnification = 2.0		Magnification = 1.5	
Magnification	Spatial Resolution (lp/mm)	Source Size (mm^2)	Spatial Resolution (lp/mm)	Pixel Size (mm^2)	Spatial Resolution (lp/mm)
1	1	0.3×0.3	2	0.15×0.15	2
1.5	2	0.1×0.1	4	0.1×0.1	5
2	4			0.0625×0.0625	6

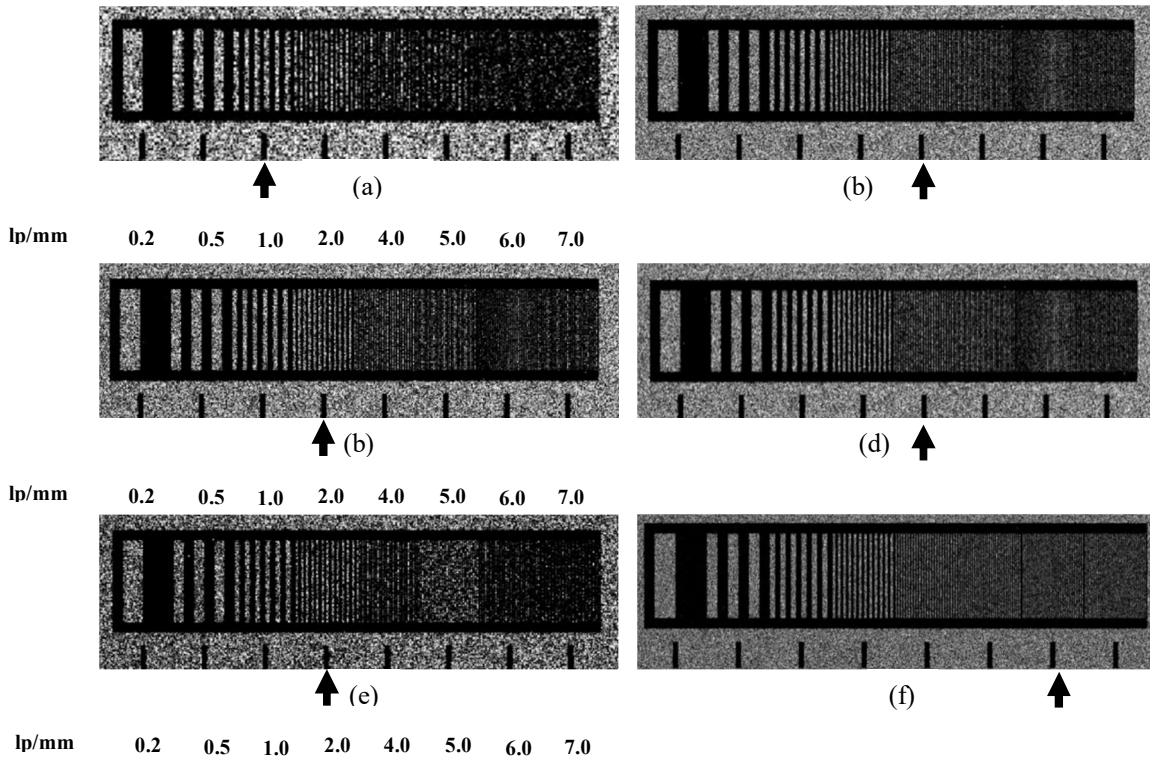


FIG. 9. Images of the line pair phantom are shown. Figures 9(a) and 9(b) show images with a pixel size of 0.15 mm, a source size of 0.1 mm, and magnifications that vary from 1.0 to 2.0, respectively. Figs. 9(c) and 9(d) show images with a magnification of 2.0, pixel size of 0.15 mm, and source size that varied from 0.3 to 0.1 mm, respectively. Figures 9(e) and 9(f) show images with a magnification of 1.5, source size of 0.1 mm, and pixel size that varied from 0.15 to 0.0625 mm, respectively. The shown arrow indicates the visual assessment of the spatial resolution in lp/mm for each simulation.

This research proved that air gap is a good technique in removing scatter radiation and thus is expected to improve image contrast. On one side, the air gap causes magnification, which may improve the effective spatial resolution of the image receptor, allowing for more samples (pixels) of small objects. On the other side, the air gap forces the images to be magnified and

may cause the loss of spatial resolution due to blurring. The latter effect may be minimized by using a small source size. In addition, using an air gap causes the image of the breast to be large, which may require a larger image receptor than what is available.

3.4. Comparison of Scatter Removal Techniques

Table 10 and Fig. 10 clearly show that the anti-scatter grid has a higher percent scatter removal than the air gap. With a GR of 2:1, the percent scatter removal was 68.6% with a gradual increase reaching above 90% with a GR of 8:1. However, the percent scatter removal with a magnification of 1.2 was only 8.3% and increased to 76.9% with a magnification of 2.0. In addition, Table 10 and Fig.10 compare the increase in radiation absorbed dose through the Bucky factor for ASG and the air gap dose factor

for AG. The increase in radiation absorbed dose was lower with the air gap than the ASG until the magnification of 1.8. For a magnification of 2.0, the situation reversed, and the AGDF was higher than the Bucky factor of anti-scatter for all grid ratios. In general, ASG is more effective in removing scatter radiation than AG, but it may cause more radiation absorbed dose. Our recommendation is to be extremely careful when using a 2.0 magnification as well as high GR because the radiation absorbed may be increased by several folds (see Fig. 10 and Table 10).

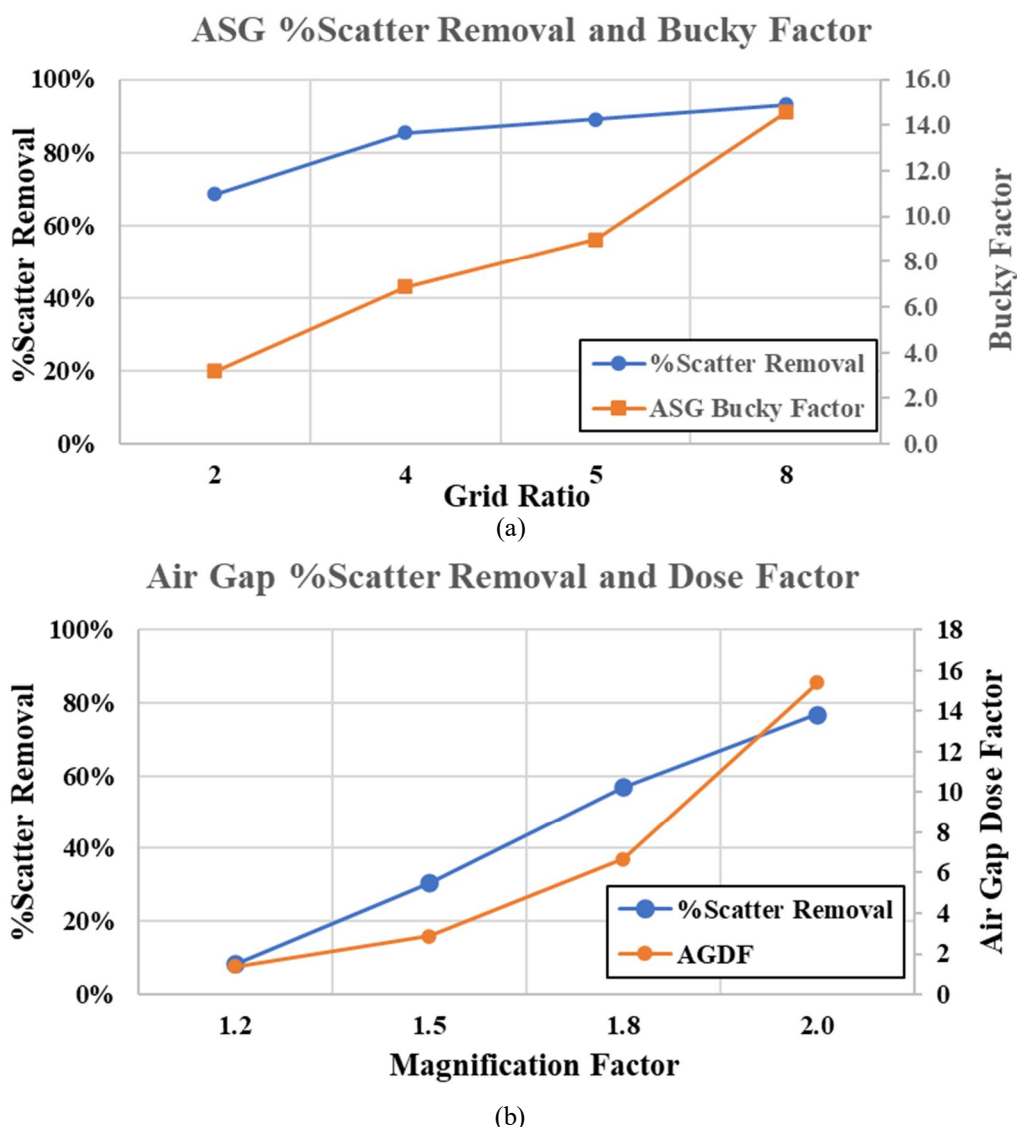


FIG. 10. These graphs compare the %scatter removal and dose factor in the anti-scatter grid and air gap technique. These factors are (a) for the anti-scatter technique and (b) for the air gap technique.

TABLE 10. The percent scatter removal and dose factor between the anti-scatter grid and air gap techniques are compared. Some results were taken from Table 5 and Table 8.

NWoG	Anti-scatter Grid Technique				Magnification	Air Gap Technique		
	GR	NWG	%SR	BF		NWAG	%SR	AGDF
1775808	2	556986	68.6%	3.2	1.2	1628025	8.3%	1.4
	4	258717	85.4%	6.9	1.5	1233111	30.6%	2.9
	5	195328	89.0%	9.0	1.8	763247	57.0%	6.7
	8	122008	93.1%	14.6	2	409407	76.9%	15.4

NWoG number of photons reached the image receptor without a grid or air gap

NWG number of photons reached the image receptor with the anti-scatter grid

NWAG number of photons reached the image receptor with the air gap

GR is the grid ratio, BF is the Bucky Factor, AGDF is the air gap dose factor

%SR is the percent of scatter removal = $(\text{NWoG} - [\text{NWG or NWAG}] \times 100 / \text{NWoG}$

4. Conclusion

X-ray mammography uses lower energy X-ray photons to obtain and enhance contrast between breast tissues. Although the photoelectric effect is the dominant tissue X-ray interaction at low energy photons, there are other types of X-ray scatter a radiation tissue interaction that cause reduction in the image contrast. Therefore, scatter radiation removal techniques are essential for enhancing breast tissue contrast.

This research was able to successfully simulate with Monte Carlo simulation via Geant4 the two main techniques, the anti-scatter grid (ASG) and the air gap (AG). These techniques are typically used in minimizing X-ray scatter radiation. Common filtered X-ray mammography spectrums were successfully modeled by Gaussian spectrums that provided similar half-value layers. These modeled spectrums were used in evaluating the ASG and the AG techniques to irradiate an acrylic mammographic simulated phantom.

The Bucky factor of ASG was used in evaluating the effectiveness of removing X-ray scatter radiation and evaluating the increase in radiation absorbed dose. This research also studied the influence of septa spacing in removing scattering radiation while keeping the grid ratio and the grid frequency constant. As septa spacing decreased, higher radiations were removed. The grid frequency was another factor that influenced the ASG's effectiveness in scatter radiation removal. The grid frequency may slightly decrease or increase the Bucky factor depending on whether the grid ratio is kept constant or variable. Despite the clear

benefits of the ASG, it may cause periodic and shadowing artifacts. This research proved that designing ASG with high GF (80 lp/mm) and low GR (2:1) minimizes the possibility of these artifacts. In addition, orienting ASG parallel to the chest-nipple axis reduces the shadowing artifact.

Furthermore, this research validated the effectiveness of using air gap in removing X-ray scatter radiation through the use of air gap dose factor (AGDF). AGDF increased with increasing air gap (magnification). The difference in AGDF between the modeled X-ray spectrums was clearly apparent at the highest simulated magnification of 2.0. This research cautions against the usage of high magnification due to the possible large increase in radiation absorbed dose. Although air gap was validated to be an effective technique in removing scatter radiation, it may cause blurring within the image due to the focal spot size. Thus, using a smaller focal spot size (e.g. $0.1 \times 0.1 \text{ mm}^2$) with increasing magnification not only reduces the blurring but also improves the effective image receptor spatial resolution.

By comparing the usage of AG with ASG, it was found that ASG was more effective in removing scatter radiation, albeit at the expense of higher radiation absorbed dose exposure. However, there is an exception observed with higher magnification (e.g. magnification = 2.0), where the air gap dose factor may exceed the Bucky factor of the ASG. Our recommendation is to be extremely careful when using high magnification, as well as a high grid ratio, due to the significant increase in the radiation absorbed dose.

References

- [1] Arleo, E.K., Hendrick, R.E., Helvie, M.A. and Sickles, E.A., *Cancer*, 123 (2017) 3673.
- [2] Zubor P., Kubatka P. et al., *Int. J. Mol. Sci.*, 20 (2019) 2878.
- [3] Bushberg, J.T., Seibert, J.A., Leidholdt Jr, E.M. and Boone, J.M., "The Essential Physics of Medical Imaging", 3rd Ed., (Lippincott Williams & Wilkens, 2012).
- [4] Shrestha, S., Vedantham, S. and Karellas, A., *Med. Phys.*, 43 (2016) 3716.
- [5] Mowlavi, A.A., *Iran. J. Radiat. Res.*, 3 (2016) 129.
- [6] Alyassin, A.M., Maqsoud, H.A., Mashat, A.M., Al-Mohr, A.-S. and Abdulwajid, S., *Appl. Radiat. Isot.*, 72 (2013) 16.
- [7] Martin, A., Gebiski, E.V. and Baldock, C., *Phys. Eng. Sci. Med.*, 44 (2021) 997.
- [8] Sarrut, D. et al., *Phys. Med. Biol.*, 66 (2021) 10.
- [9] Sarrut, D., Bardiès, M., Bousson, N. et al., *Med. Phys.*, 41 (2014) 64301.
- [10] Morris, R., Lakshmanan, M., Fong, G., Kapadia, A. and Greenberg, J., *Med. Phys.*, 43 (2016) 3398.
- [11] Tirao, G., Quintana, C. and Valente, M., *Int. J. Low Radiation*, 7 (2010) 276.
- [12] Taha, E.M. and Alyassin, A.M., *Insights Med. Phys.*, 1 (2016) 1.
- [13] Taha, E.M., Alhawsawi, A., Siddig, M. and Balamesh, A.S., *Arab. J. Sci. Eng.*, 47 (2022) 7583.
- [14] Abolaban, F.A. and Taha, E.M., *J. Radiat. Res. Appl. Sci.*, 13 (2020) 642.
- [15] Banoqitah, E., Taha, E.M., Elmoujarkach, E. and Alsharif, S., *Results Phys.*, 10 (2018) 323.
- [16] Alyassin, A.M., *Int. J. Med. Phys. Clin. Eng. Radiat. Oncol.*, 11 (3) (2022) 135.
- [17] Leon, S.M., Brateman, L.F. and Wagner, L.K., *Med. Phys.*, 41 (2016) 111914.
- [18] Fedon, C., Caballo, M., Longo, R., Trianni, A. and Sechopoulos, I., *Med. Phys.*, 45 (2018) 1724.
- [19] Fedon, C., Caballo, M. and Sechopoulos, I., *Med. Phys.*, 45 (2018) 3950.
- [20] Sechopoulos, I., Suryanarayanan, S., Vedantham, S., D'Orsi, C.J. and Karellas, A., *Med. Phys.*, 34 (2007) 564.
- [21] Franco, F., Sarno, A., Mettiviera, G., Hernandez, A.M., Bliznakova, K., Boone, J.M. and Russo, P., *Phys. Med.*, 74 (2020) 133.
- [22] Lee, J., Lim, C.H., Park, J.W., Kim, I.H., Moon, M.K. and Lim, Y.K., *J. Radiat. Prot. Res.*, 42 (2017) 197.
- [23] Marimón, E., Marsden, P.A., Nait-Charif, H. and Díaz, O., *Phys. Med. Biol.*, 66 (2021) 14.
- [24] Rasband, W.S., ImageJ, (U.S. National Institutes of Health, Bethesda, Maryland, USA, 1997-2018), <https://imagej.nih.gov/ij/>.
- [25] Rueden, C.T., Schindelin, J., Hiner, M.C. et al., *BMC Bioinform.*, 18 (1) (2017) 529.